# A New Approach to Model-Based Simulation of Disordered Polymer Blend Solar Cells

Stenzel, Ole; Koster, L. Jan Anton; Thiedmann, Ralf; Oosterhout, Stefan D.; Janssen, Rene A. J.; Schmidt, Volker

*Published in:*
Advanced Functional Materials

*DOI:*
10.1002/adfm.201102095

FULL PAPER

# A New Approach to Model-Based Simulation of Disordered Polymer Blend Solar Cells

*Ole Stenzel, L. Jan Anton Koster, Ralf Thiedmann, Stefan D. Oosterhout, René A. J. Janssen,* and Volker Schmidt**

**The 3D nanomorphology of blends of two different (organic and inorganic) solid phases as used in bulk heterojunction solar cells is described by a spatial stochastic model. The model is fitted to 3D image data describing the photoactive layer of poly(3-hexylthiophene)-ZnO (P3HT-ZnO) solar cells fabricated with varying spin-coating velocities. A scenario analysis is performed where 3D morphologies are simulated for different spin-coating velocities to elucidate the correlation between processing conditions, morphology, and efficiency of hybrid P3HT-ZnO solar cells. The simulated morphologies are analyzed quantitatively in terms of structural and physical characteristics. It is found that there is a tendency for the morphology to coarsen with increasing spin-coating velocity, creating larger domains of P3HT and ZnO. The impact of the spin-coating velocity on the connectivity of the morphology and the existence of percolation pathways for charge carriers in the resulting films appears insignificant, but the quality of percolation pathways, considering the charge carrier mobility, strongly varies with the spin-coating velocity, especially in the ZnO phase. Also, the exciton quenching efficiency decreases significantly for films deposited at large spin-coating velocities. The stochastic simulation model investigated is compared to a simulated annealing model and is found to provide a better fit to the experimental data.**

## 1. Introduction

Organic and hybrid solar cells are a promising alternative to classical silicon solar cells, being cheap in production and ecological. However, despite enormous improvements, they still suffer from relatively low efficiencies. Up to now, the most efficient organic solar cells reach power conversion efficiencies of about 7–8%.[1] In organic solar cells the efficiency depends on the close intermixture of the electron-donor and electron-acceptor materials to generate charges and on the presence of unhindered percolation pathways to transport these charges towards the electrodes. The nanomorphology of these bulk heterojunction solar cells is strongly influenced by the processing conditions used in depositing the photoactive layer. Drying time, nature of the solvent, processing agents, and thermal annealing are just a few of the many parameters that have been used to control the extent of mixing and the size and interconnectivity of domains of donor and acceptor materials and thereby the efficiency.[2–4] Unfortunately, a quantitative understanding of the relation between processing parameters, morphology, and efficiency is largely missing.

To better understand the relation between nanomorphology and efficiency, we recently developed a spatial stochastic simulation model for the morphology of organic solar cells.[5] This multiscale sphere model (MSM) has been fitted to high-resolution 3D electron tomography data describing the morphology of photoactive layers of poly(3-hexylthiophene)-ZnO (P3HT-ZnO) solar cells. These P3HT-ZnO layers are fabricated using an in situ sol-gel method in which the ZnO phase is formed from a molecular precursor during spin-coating.[6] The corresponding solar cells provide a power conversion efficiency up to 2% in simulated solar light. By varying spin-coating velocities, film thickness, nanomorphology, and efficiency of the P3HT-ZnO layers can be influenced.[6] Here, we correlate the parameters of the multiscale sphere model to the spin-coating velocity during deposition of the layer. We demonstrate that it is possible to accurately mimic the results of the spin-coating process for the considered material combination (P3HT-ZnO) and simulate morphologies of photoactive layers with arbitrary spin-coating velocity. A scenario analysis is performed in which morphologies are simulated and analyzed for varying spin-coating velocities. It turns out that the morphology becomes coarser for increasing spin-coating velocity $\omega$, especially for $\omega > 4000$ rpm,

O. Stenzel, Dr. R. Thiedmann, Prof. V. Schmidt
Institute of Stochastics
Ulm University
Ulm, 89069, Germany
E-mail: volker.schmidt@uni-ulm.de
Dr. L. J. A. Koster
Molecular Electronics
Zernike Institute for Advanced Materials
University of Groningen
Groningen, 9747 AG, The Netherlands
S. D. Oosterhout, Prof. R. A. J. Janssen
Chemical Engineering and Chemistry
Molecular Materials and Nanosystems
Eindhoven University of Technology
Eindhoven, 5600 MB, The Netherlands
E-mail: r.a.j.janssen@tue.nl

DOI: 10.1002/adfm.201102095

such that larger domains of both polymer and ZnO evolve. In particular, the spherical contact distances (defined as the closest distance from a randomly chosen point in one component to the other component) from P3HT to ZnO increase for increasing $\omega$. This causes a decrease in the efficiency by which excitons generated in P3HT are quenched at the P3HT/ZnO interface and dissociate into holes and electrons. More precisely, the calculated exciton quenching efficiency (excitons quenched by ZnO in the presence of electrodes) decreases from 0.79 for $\omega = 1000$ rpm to 0.18 for $\omega = 5250$ rpm (see Section 4.2.2). Surprisingly, the extent to which the electron acceptor (ZnO) phase is connected to the electron collecting electrode remains more or less constant for all considered $\omega$, with a value close to 100%, although the layer thickness strongly varies for $\omega$.[7]

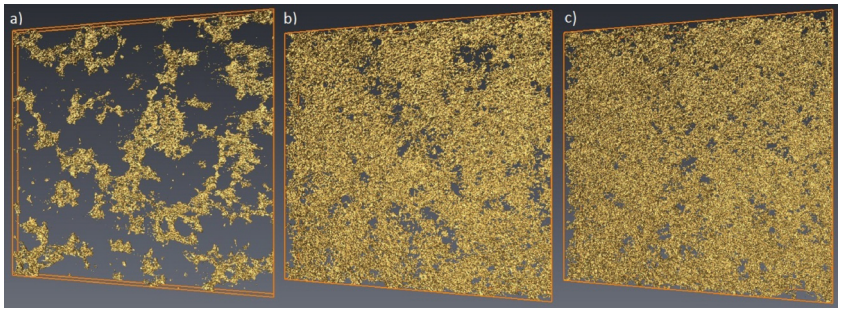


**Figure 1.** Reconstructed 3D electron tomography volume images for P3HT-ZnO blends prepared at different spin-coating velocities, showing the ZnO volume in yellow with P3HT being transparent against a black background: a) 57 nm ($\omega = 5000$ rpm), b) 100 nm ($\omega = 1500$ rpm), and c) 167 nm ($\omega = 1000$ rpm). The size of the three images is about 700 × 700 nm$^2$ in the $x$–$y$ plane.

The multiscale sphere model is compared to simulated annealing, a well-established method to simulate morphologies in organic solar cells, see e.g. Peumans et al.[8] It turns out that simulated annealing underestimates spherical contact distances from P3HT to ZnO, which yields an overestimation in terms of quenching efficiency. Moreover, morphologies generated by simulated annealing, in contrast to MSM, have a significantly worse connection with the electrodes than observed in the experimental data.

The paper is organized as follows. In Section 2, the data to which the multiscale sphere model has been fitted is briefly described. Next, in Section 3, the multiscale sphere model developed by Stenzel et al. is summarized and the model parameters are correlated to the spin-coating velocity $\omega$.[5] In Section 4, a scenario analysis of morphologies simulated for a number of spin-coating velocities, is performed. Section 5 compares MSM to simulated annealing. Finally, in Section 6, the results are summarized.

## 2. Experimental Image Data

The 3D images of the photoactive layer of the solar cells were obtained by electron tomography.[9] In the present study we use three different morphologies recorded for P3HT-ZnO layers with thicknesses of 57 nm ($\omega = 5000$ rpm), 100 nm ($\omega = 1500$ rpm), and 167 nm ($\omega = 1000$ rpm), see **Figure 1**. More information regarding the experimental data can be found in ref. [6].

## 3. Simulation Model for the Morphology of Polymer-ZnO Solar Cells

The 3D stochastic simulation model we recently developed for the morphology of P3HT-ZnO solar cells is based on tools from stochastic geometry and spatial statistics.[5] In particular, various classes of so-called marked point processes are used, see e.g., Stoyan et al. and Illian et al. for an introduction to these fields.[10,11] First, a data preprocessing is performed,[12] where the complexity of the solar cell morphology data to which the model will be fitted is split into two different length scales, the macro- and the microscale (**Figure 2**a). The macroscale, which is obtained by morphological smoothing, contains the main structural features of the ZnO phase. The microscale consists of all details that were omitted on the macroscale. Subsequently, a stochastic simulation model is developed for each scale individually. By this partitioning of complexity, a very flexible model has been obtained. The composition of the models for the macro- and the microscale is the final 3D simulation model, which we call a multiscale sphere model (MSM).

### 3.1. Simulation Model for the Macroscale

The basic idea is to represent the ZnO domains on the macroscale as a system of overlapping spheres. Therefore, a sphere-putting algorithm is applied to the experimental image data.[12]

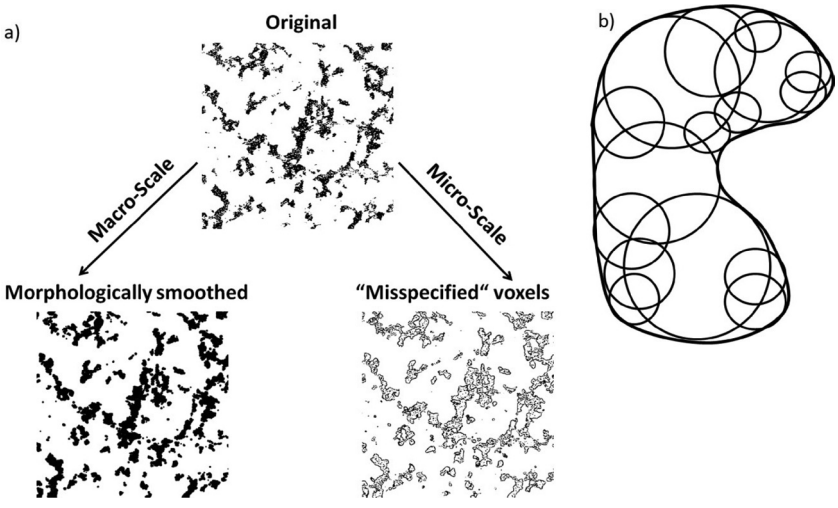


**Figure 2.** a) Original image split up into structural components at two different length scales (macroscale and microscale). b) Schematic 2D representation of a ZnO domain by union of circles.

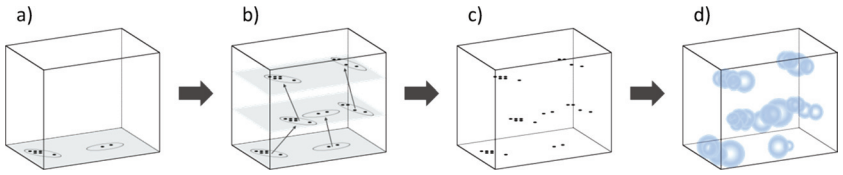


**Figure 3.** a) First 2D slice of points. b) Displacement of clusters, including spatial birth and death. c) Resulting 3D point pattern. d) 3D morphology by union of overlapping spheres.

It represents the morphologically smoothed ZnO domains in an efficient way by unions of overlapping spheres as schematically illustrated in Figure 2b. This representation allows interpreting the ZnO domains as a realization of a marked point process, where the points are the sphere centers and the marks the corresponding radii. For more information on marked point processes, see Illian et al.[11] After a thorough analysis of the point patterns for the 57, 100, and 167 nm films, a suitable point-process model has been developed that is parameterized and sufficiently flexible to represent all three film thicknesses, i.e., the model type is the same for all three film thicknesses with varying parameters indicating different morphological structures.

Briefly, the point-process model for the macroscale is as follows: a 3D point process is constructed as a sequence of identically distributed 2D point processes, where the 2D processes are modeled by elliptical Matérn cluster processes (**Figure 3**a), see ref. [10] for a formal definition. More precisely, we start with the first 2D slice and put ellipses with random location and random orientation in the $x$–$y$ plane of the observation window (in the plane of the substrate). Secondly, so-called descendant or child points are placed at random inside the ellipses. Subsequent 2D slices are obtained as stochastic modifications of their predecessors (Figure 3b). The stochastic modifications include a lateral shift of each cluster (i.e., ellipse with child points) in the $x$–$y$ plane and a birth-and-death process, i.e., clusters can be "born" or "die". The intensity of the birth-and-death process gives control to adjust the connectivity of the simulated morphologies, where a higher intensity yields a lower connectivity. Subsequent slices are added according to the same rules until the thickness of the considered film is reached. At the end, the totality of child points is taken as a point pattern of sphere centers (Figure 3c). In a final step, spheres are put around every child point where the radii follow a Gamma distribution (Figure 3d). Ref. [5] provides a more detailed description of the macroscale model.

### 3.2. Simulation Model for the Microscale

The simulation model for the microscale is used to reinsert all details omitted on the macro-scale. In particular, we differentiate three types of microscale components: a) outer misspecifications (typically small isolated ZnO particles in the polymer phase), b) interior misspecifications (isolated areas of polymer in the ZnO phase), and c) boundary misspecifications (typically thin branches of ZnO at the phase boundary). For each of these components, a suitable model has been developed. First, outer misspecifications are modeled by a marked point process (sphere systems), see **Figure 4**a,b. Secondly, the boundary misspecifications are modeled by an erosion in dependence of the outer misspecifications (Figure 4c). Finally, interior misspecifications are added by a marked point process (Figure 4d). For details, see ref. [5,9].

### 3.3. Model Fitting

To fit the point-process model to experimental data and determine the parameters of the model we use a minimum contrast method that is widely applied in the literature.[10,11] Therefore, morphologies are simulated in dependence of a parameter vector $\vec{\lambda} = (\lambda_1, \ldots, \lambda_m)$ for some $m \geq 1$. Subsequently, image characteristics $F(\vec{\lambda})$ of simulated data are compared to their experimental counterparts $\hat{F}$ estimated from the image data. The parameter vector $\vec{\lambda}$, which minimizes the discrepancy between these image characteristics, defined as the norm $\| F(\vec{\lambda}) - \hat{F} \|$, is chosen as a so-called minimum-contrast estimate, i.e.,

$\vec{\lambda} = \{\vec{\lambda} \mid \| F(\vec{\lambda}) - \hat{F} \| \text{ minimal}\}$, where $\| F(\vec{\lambda}) - \hat{F} \|$ denotes a certain modified Lévy distance between $F(\vec{\lambda})$ and $\hat{F}$ (see ref. [5] for details).

### 3.4. Model Validation

**Figure 5** shows a cutout of the experimental data accompanied by a corresponding simulation and gives an impression of the goodness-of-fit that the multiscale sphere model offers. It is important to note that because we consider a stochastic simulation model it is not intended to match the experimental data, but to match their structural characteristics.

Before the model can be applied to improve the understanding of solar cells, it must be assured that it reflects physical properties sufficiently well. Therefore, we compute physically relevant characteristics, such as exciton quenching efficiency, connectivity (defined as the fraction of ZnO material connected with the electron collecting top metal electrode), and relative charge carrier mobilities for both phases (P3HT and ZnO) for experimental and simulated data, respectively.

The charge carrier mobility in each phase of the binary blend is calculated by considering the transport of charges to be restricted to the respective phase. The voxels (volumetric picture elements) that make up this phase are treated as hopping sites. Energetic disorder is taken into account by using a Gaussian density of states of width 75 meV, which is typical for materials used in organic solar cells. More details can be found


**Figure 4.** Modeling of microscale. a) Macroscale (cutout). b) Outer misspecifications added. c) Boundary misspecifications corrected. d) Interior misspecifications added.

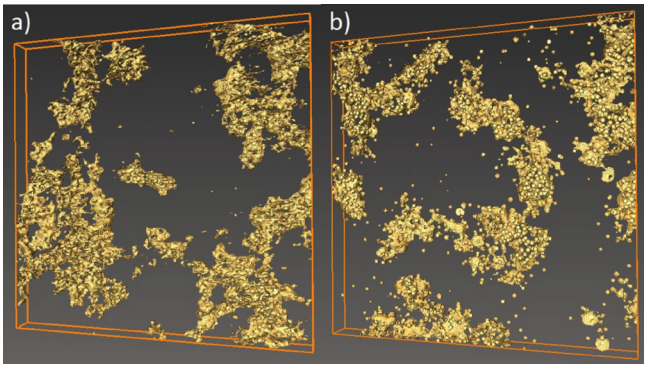


**Figure 5.** Volume images of P3HT-ZnO a) Experimental 3D morphology of the 57 nm film (cutout). b) Simulated 3D morphology of fitted model for the 57 nm film (cutout). In the images the ZnO volume is yellow and P3HT is transparent against a black background.

in ref. [13]. Dividing the so-obtained mobility by the mobility of unblended neat material yields the relative mobility.

We define the quenching efficiency $\eta_Q$ as the probability of an exciton that is located at random in the P3HT phase to reach the interface with the ZnO, where the exciton dissociates into charge carriers. It is obtained from the field $n(x)$ of local exciton densities in the P3HT phase. The field $n(x)$ is determined by solving the steady-state diffusion equation

$$0 = \frac{\mathrm{d}n(x)}{\mathrm{d}t} = \frac{-n(x)}{\tau} + D\nabla^2 n(x) + g$$

which describes the diffusion of excitons, where $D$ is the diffusion constant, $\tau$ is the exciton lifetime, and $g$ is the rate of exciton generation. The values for the exciton lifetime ($\tau = 400$ ps) and the exciton diffusion constant ($D = 1.8 \times 10^{-7}$ m$^2$ s$^{-1}$) are taken from the literature.[14] Exciton quenching by ZnO is taken into account by requiring $n(x) = 0$ at the polymer/ZnO interface. Cyclic boundary conditions are applied in all directions. The simulation volume contained 68 million, 121 million, and 193 million grid points for the 57, 100, and 167 nm films, respectively. The exciton quenching efficiency is then obtained by $\eta_Q = 1 - \bar{n}/(\tau g)$, where $\bar{n}$ describes the average exciton density.[5,6]

The results displayed in **Table 1** reveal an excellent correspondence between the experimental and simulated (MSM) morphologies for most of the considered characteristics, where "±" describes the standard error. Only the values for the mobility in the simulated ZnO phase for the 100 nm and 167 nm films and the connectivity for the 57 nm film differ from the original values computed for experimental image data.

### 3.5. Parameter Regression

The developed simulation model is fully parameterized. This means that a given solar cell morphology is characterized by the corresponding parameter vector $\vec{\lambda}$ of the model.

At first, in extension of the three solar cell morphologies considered so far, the model is fitted to three more solar cell morphologies with film thicknesses of 87 nm ($\omega = 4000$ rpm), 89 nm ($\omega = 2000$ rpm), and 124 nm ($\omega = 1500$ rpm). Thus, altogether the model has been fitted to six different solar cell morphologies fabricated with varying spin-coating velocities $\omega_i$, $i = 1, \ldots, 6$, and keeping all other experimental parameters fixed. Therefore, in our setting, $\omega$ is the variable determining the solar cell morphology and therefore also determining the parameter vector $\vec{\lambda}$. Hence, we interpret the parameter vector $\vec{\lambda}$ as a function of $\omega$, i.e., $\vec{\lambda} = \vec{\lambda}(\omega)$, from which six estimated points of support $\{\hat{\vec{\lambda}}(\omega_i), i = 1, \ldots, 6\}$ are given. In the following, a regression for $\lambda(\omega) = (\lambda_1(\omega), \ldots, \lambda_m(\omega))$ is developed, where for each component $\lambda_j(\omega)$ individually, either a linear model or a shifted exponential model of type $\lambda_j(\omega) = a_j + b_j \exp(c_j\omega) + \varepsilon_j$ is used. **Figure 6** shows the regression of the macroscale model parameters. Note that the curves of Figure 6 are suitably rescaled to fit into a common graph. As can be seen from Figure 6, the regression models fit the data quite well. The regression models for the parameters of the microscale model are analogous. The advantage of these regression models is that solar cell morphologies for any arbitrary spin-coating velocity $\omega$ can be generated and subsequently analyzed. Such a scenario analysis is performed in Section 4.

## 4. Scenario Analysis

To improve the understanding of how the spin-coating velocity influences the morphology and, in turn, how morphology affects device performance, a series of morphologies are simulated using the stochastic simulation model (MSM) as described in Section 3. The parameters are chosen according to the regression models of Section 3.5.

### 4.1. General Setting

For each spin-coating velocity $\omega = 500, 750, \ldots 5250$ rpm, ten virtual morphologies have been simulated. The voxel resolution of 0.71 nm corresponds to the experimental morphology data described in Section 2. Since the thickness of the photoactive

**Table 1.** Characteristics of experimental and simulated (MSM) morphologies.

| Film thickness | | Connectivity | Exciton Quenching | Relative Mobility (polymer phase) | Relative Mobility (ZnO phase) |
|---|---|---|---|---|---|
| 57 nm | Exp. | 0.97 | 0.43 | 0.88 | 0.32 |
| | MSM | 0.93 ± 0.01 | 0.42 ± 0.03 | 0.89 ± 0.01 | 0.31 ± 0.01 |
| 100 nm | Exp. | 0.98 | 0.80 | 0.76 | 0.16 |
| | MSM | 0.98 ± 0.01 | 0.81 ± 0.01 | 0.76 ± 0.02 | 0.19 ± 0.01 |
| 167 nm | Exp. | 0.97 | 0.81 | 0.77 | 0.15 |
| | MSM | 0.96 ± 0.01 | 0.83 ± 0.01 | 0.73 ± 0.01 | 0.11 ± 0.01 |

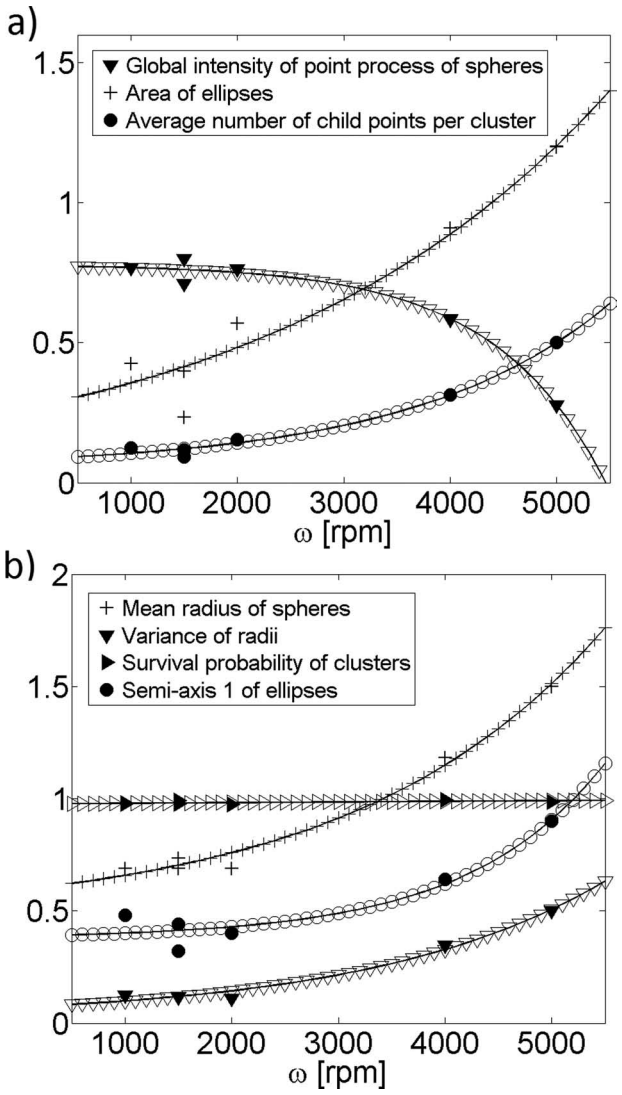


**Figure 6.** Regression of model parameters of the macroscale. The open symbols display the regression curves, where the estimated parameters from the experimental data are added by solid symbols.

layer also depends on the spin-coating velocity $\omega$, a regression model for the layer thickness is fitted to the P3HT-ZnO solar cells. Following Norrman et al.,[7] the layer thickness $h$ is given by $h = c\omega^{\alpha}$, where $\alpha = -0.5$ is chosen in most cases and $c$ is a constant.[7] Taking $\alpha = -0.5$, the method of least-squares yields $c = 4641$ nm (**Figure 7**) and hence the morphologies are simulated with a layer thickness given by $h = 4641\omega^{-0.5}$. The window size in the $x$–$y$ plane is chosen fixed with 909 × 932 voxels, which is in accordance with the experimental image data.

### 4.2. Results

**Figure 8** displays cutouts of simulated morphologies for varying spin-coating velocities and gives an impression how the solar cell morphology is influenced by the spin-coating velocity. With increasing $\omega$, the morphology has larger phase-separated

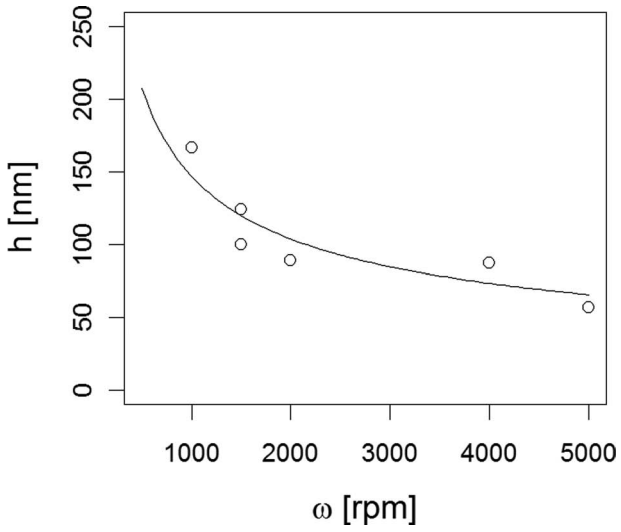


**Figure 7.** Film thickness $h$ vs. spin-coating velocity $\omega$. The line displays the regression curve and the open circles represent the layer thicknesses from the experimental data.

domains of both P3HT and ZnO and, therefore, is more clustered. The same trend has also been observed in the experimental image data obtained by electron tomography.[6] In particular, the morphology changes dramatically for $\omega >$ 4000 rpm. In the following, several structural and physical characteristics are computed and analyzed for the series of simulated morphologies, where in **Figure 9–11** values from the scenario analysis are displayed by open circles and values for experimental image data are added as filled circles.

#### *4.2.1. Structural Characteristics*

At first, the volume fraction of ZnO is considered (Figure 9a). It turns out that the volume fraction remains at about 20% for $\omega < 4250$ rpm. Beyond that, the volume fraction decreases dramatically to about 6.0% at 5250 rpm. Experimentally this can be understood by considering that the molecular ZnO precursor, diethylzinc, used for making the blends is volatile and partly evaporates during film formation. Evidently, this occurs more rapidly at higher spin-coating velocities where films are thin. Note that the discontinuity in Figure 9a at $\omega = 2750$ rpm is due to discretization issues that arise when working on a discrete lattice of voxels. Next, we consider the mean spherical contact distance from polymer to ZnO,[10] i.e., the average shortest distance from a randomly chosen polymer voxel to the ZnO phase. Note that spherical contact distances of the experimental image data

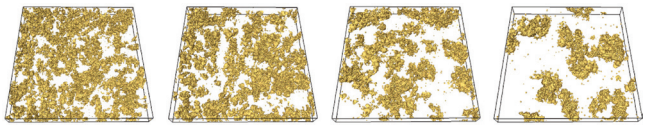

**Figure 8.** Cutouts of simulated P3HT-ZnO morphologies for $\omega = 1000$, 2500, 4000, and 5000 rpm (from left to right) and window size 355 × 355 × 28.4 nm$^3$. In the images the ZnO volume is yellow and P3HT is transparent against a white background.

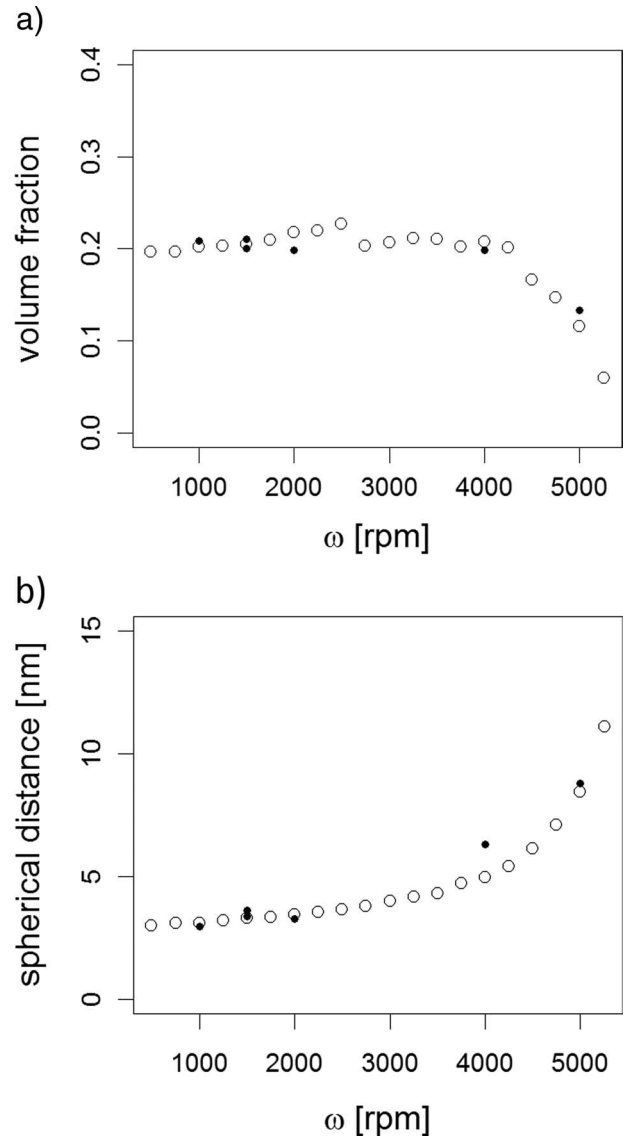


**Figure 9.** a) Volume fraction of ZnO vs. $\omega$. b) Mean spherical contact distance from polymer to ZnO vs. $\omega$. The open circles represent the data for the simulated morphologies and solid circles the data for the experimental morphologies.

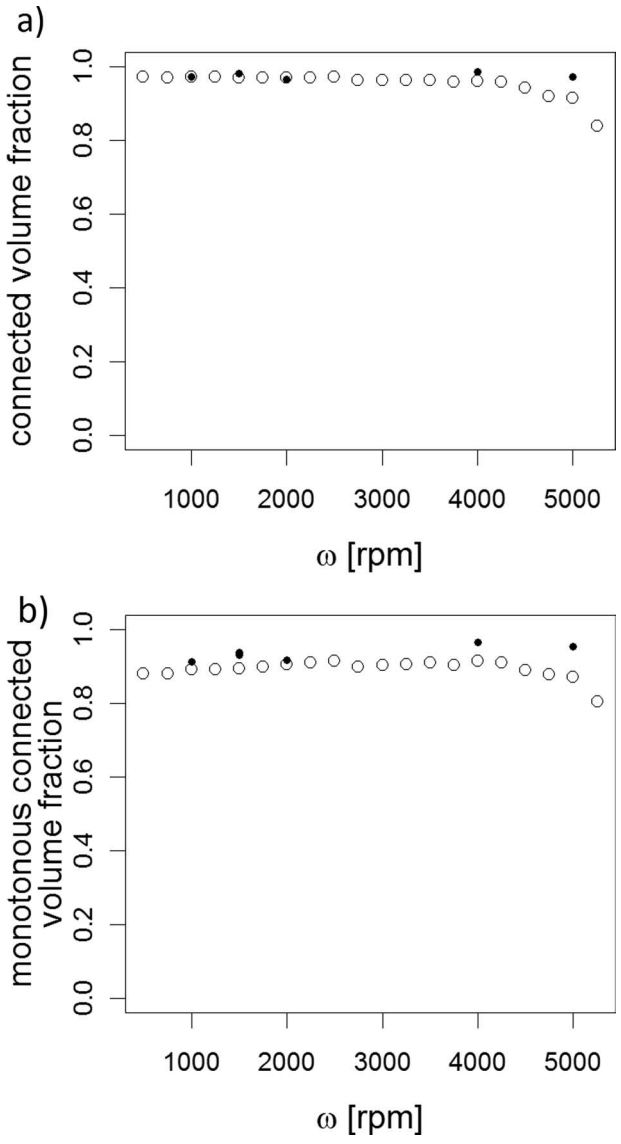


**Figure 10.** a) ZnO volume fraction connected to the top electrode. b) ZnO volume fraction connected monotonically (i.e., through a strictly rising path) to the top electrode. The open circles represent the data for the simulated morphologies and solid circles the data for the experimental morphologies.

have already been considered previously.[6] Since the exciton diffusion length is just a few nanometers,[14] large spherical contact distances are unfavorable for the solar cell efficiency due to a poor exciton quenching efficiency. As shown in Figure 9b, the mean spherical contact distance is monotonically increasing if $\omega$ increases and that a strong increase can be observed for spin-coating velocities $\omega > 4250$ rpm. This is due to the strong clustering of ZnO and the relatively small volume fraction of ZnO. Thus, many excitons in solar cells prepared with $\omega > 4250$ rpm will not be quenched at the P3HT-ZnO interface.

The solar cell efficiency also depends on the presence of unhindered percolation pathways for charges to diffuse or drift towards the electrodes. The percolation of the ZnO phase is considered in Figure 10 as the connectivity (defined as the fraction of ZnO material connected with the electron collecting top metal electrode) and the monotonic connectivity (defined as the fraction of ZnO material connected to the electron collecting top metal electrode through a strictly rising path). Note that the connectivity of experimental image data has already been considered by Oosterhout et al.,[6] where not all slices of the 3D images could be used for analysis due to the relatively rough surface of the active layer. The virtual morphologies are simulated with the correct size in $z$-direction, which is computed according to the function shown in Figure 7. This yields more accurate information on the connectivity. Figure 10a states that the connectivity remains more or less constant at values close to 100% for $\omega < 4250$ rpm and slightly decreases for $\omega \geq 4250$ rpm. This decrease in connectivity is caused

by the strong decrease in volume fraction of ZnO (see Figure 9a).

Similar, the monotonic connectivity is also very high with values close to 90%. It is quite remarkable that the (monotonic) connectivity does not vary that much with the spin-coating velocity, although the film thickness considerably varies with the spin-coating velocity. For instance, the (monotonic) connectivity is almost the same for $\omega = 1000$ rpm (film thickness: 147 nm) and $\omega = 4000$ rpm (film thickness: 73 nm). Overall, it seems that the existence of percolation pathways (monotonic or non-monotonic) in the ZnO phase towards the electron collecting metal electrode is not the limiting factor for this type of solar cell.

#### 4.2.2. Physical Characteristics

We have seen in Section 3.4 that exciton quenching efficiency is very sensitive to differences in morphology. In solar cells, apart from being quenched by ZnO, excitons can also be quenched by the electrodes constituting a loss mechanism in these devices.[6] In this scenario analysis this quenching effect is taken into account by requiring $n(x) = 0$ at the polymer/electrode interface while cyclic boundary conditions are used in the lateral directions. In this way the number of excitons that are quenched at the electrodes is easily quantified.

Figure 11a shows that the efficiency of exciton quenching by ZnO initially decreases monotonically with increasing $\omega$, but that for $\omega > 4250$ rpm a much stronger decrease sets in. This is in accordance with previous results, i.e., that the morphology becomes coarser and that the spherical contact distances increase. For thin active layers, exciton quenching at the electrodes cannot be ignored. In accordance, Figure 11b reveals that the fraction of excitons quenched by the electrodes increases for increasing $\omega$. The reasons for this trend are two-fold: Firstly, high $\omega$ yields thin films and exciton quenching by electrodes is more important in thin than in thick films. Additionally, high $\omega$ results in coarse morphology, which makes quenching by ZnO less efficient, so more excitons may be quenched at the electrodes.

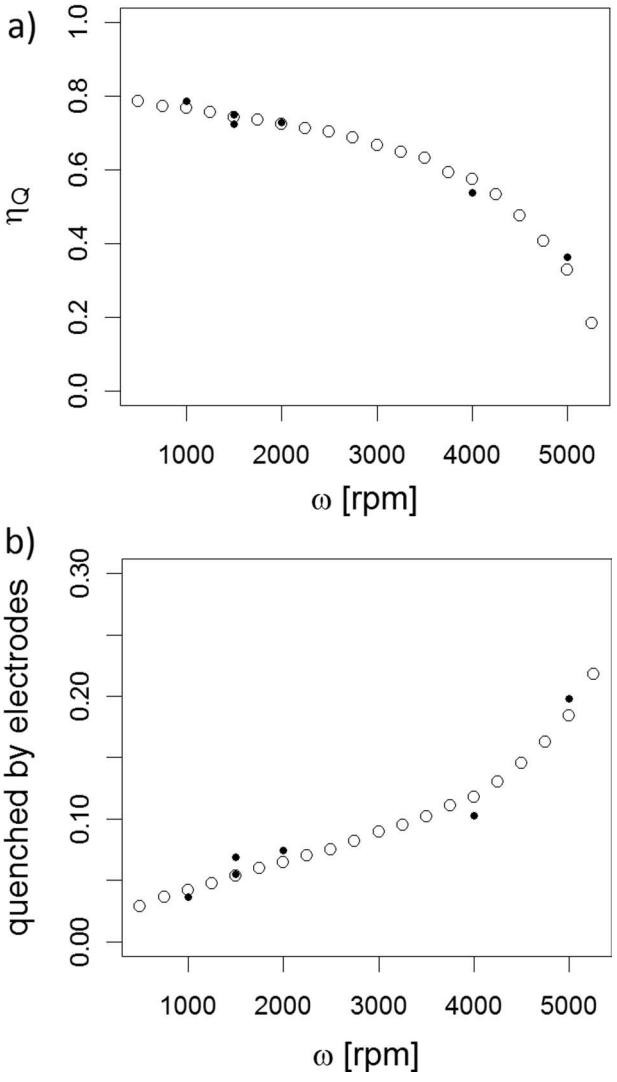


**Figure 11.** a) Exciton quenching efficiency of ZnO in the presence of electrodes. b) Excitons quenched by electrodes. The open circles represent the data for the simulated morphologies and solid circles the data for the experimental morphologies.

## 5. Comparison of the Multiscale Sphere Model to Simulated Annealing

A well-established method to generate 3D donor–acceptor morphologies is simulated annealing. Peumans et al. have used simulated annealing (SA) to describe the effects of thermal annealing on the interface morphology of a mixed-layer small molecule photovoltaic cell.[8] The basic idea is to start with a random allocation of acceptor and donor voxels (representing ZnO and P3HT) having predefined volume fractions. A Markov chain Monte Carlo algorithm is used to coarsen this blend by randomly choosing a pair of neighboring sites and probabilistically admitting a swap based on the energy of the system. As cyclic boundary conditions are used, pairwise swaps over matching faces of the morphology are also allowed. Phase separation is ensured by setting the interfacial energies of the constituent phases such that a configuration with a smaller interfacial area is lower in energy. When a predefined average feature size $\beta = 6 \min(\alpha, 1-\alpha) V/A$ is reached, where $\alpha$ is the volume fraction of ZnO, $V$ the volume of the sampling window, and $A$ the area of the interface between the phases, the simulation is stopped.

Simulated annealing is often used to generate morphologies that serve as input for further device modeling,[15,16] and it is therefore of importance to assess whether it can represent the morphology of the devices under study in a meaningful way. In the following, we compare the morphologies generated by our multiscale sphere model with those generated by SA.

As an example, both models are used to generate morphologies of ZnO volume fraction $\alpha = 0.214$ and interfacial area per volume unit $(A/V) = 0.339$ (feature size $\beta = 3.79$ voxels) so as to resemble the 167 nm solar cell film. The remaining parameters for the MSM are fixed by fitting it to the experimental 167 nm film morphology. The results given in **Table 2** show that the mean spherical contact distance is clearly underestimated by simulated annealing, which causes an overestimate in terms

**Table 2.** Characteristics of experimental and simulated (MSM and SA) morphologies for a 167 nm P3HT-ZnO film.

| | Connectivity (ZnO phase) | Mean spherical contact distance [nm] | Quenching efficiency | Relative Mobility (polymer phase) |
|---|---|---|---|---|
| Exp. | 0.97 | 3.11 | 0.82 | 0.77 |
| MSM | 0.96 | 2.94 | 0.83 | 0.74 |
| SA | 0.16 | 2.29 | 0.89 | 0.73 |

of quenching efficiency. The reason for the underestimate of spherical contact distances is that the ZnO clusters, generated by SA, are too regular compared to experimental data and thus large empty spaces are avoided. Both models reflect quite nicely the mobility in the polymer phase. The most significant difference is in the connectivity: the morphologies obtained by simulated annealing are characterized by a connectivity that is very different from the experimental one. This is also reflected in the mobility of the ZnO phase: while the MSM model still yields decent electron transport, the ZnO mobility in the SA model was too low to yield convergent simulations. Groves et al. have used SA morphologies at similar blend composition and found that the mobility is reduced by several orders of magnitude.[17] The main reason for the better fit of the MSM, especially regarding the connectivity, lies in its capability to generate anisotropic morphologies similar to the experimental data. Simulated annealing, by its implementation, generates isotropic morphologies, i.e., without preferred directions. In principle, it would be possible to include anisotropy in the SA model by introducing anisotropic side energies, but from a physical point of view that might be hard to justify. In contrast to SA, our experimental solar cell morphologies show a significant anisotropy in $z$-direction.

To show this, we consider the direction-dependent chord length distribution of the ZnO phase. In general, the chord length with respect to a line $L$ for an object $A \subset \Re^3$ is the length of the intersecting line segment $L \cap A$ (see **Figure 12**). Considering all lines with a fixed direction $\alpha$ that intersect with $A$, we can define the random chord length as the chord length of a randomly chosen line intersecting $A$. The statistical distribution of this random chord length is called chord length distribution. Intuitively speaking, the chord length distribution with respect to direction $\alpha$ is the distribution of the elongation of an object $A$ in direction $\alpha$.

Here, we consider the variance of the chord length distribution in dependence of the angle pair = $(\theta,\varphi)$ (spherical coordinates: $\theta$ inclination angle, $\varphi$ azimuthal angle), i.e., the variance of the elongation in a certain direction, is determined.[10] An isotropic morphology has a constant variance of the chord length distribution for all directions $\alpha = (\theta,\varphi)$, whereas a varying variance always indicates anisotropy. **Figure 13**a shows that the chord length variance of the experimental solar cell morphologies clearly deviates from constant variance indicating significant anisotropy. The same holds true for the multiscale sphere model (Figure 13b). In contrast, simulated annealing yields a constant variance (Figure 13c), showing its isotropy.

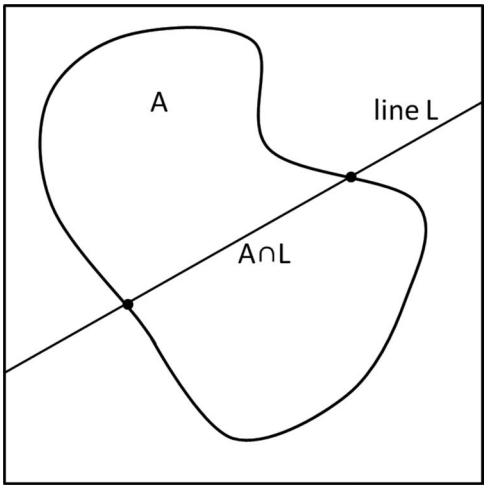


**Figure 12.** Line $L$ intersecting an object $A$.

Finally, we can conclude that for the considered system (spin-coated P3HT-ZnO), MSM describes the morphology more adequately than SA in terms of connectivity, spherical contact distances and anisotropy.

## 6. Summary and Conclusions

A stochastic multiscale sphere model[5] has been applied to study the influence of spin-coating velocity on the morphology of the photoactive layer of P3HT-ZnO solar cells. Regression models were fitted to the model parameters that were used to simulate P3HT-ZnO 3D bulk heterojunction morphologies obtained from electron tomography for layers that were deposited at six different spin-coating velocities. Subsequently, a scenario analysis was performed where morphologies were simulated for spin-coating velocities ranging

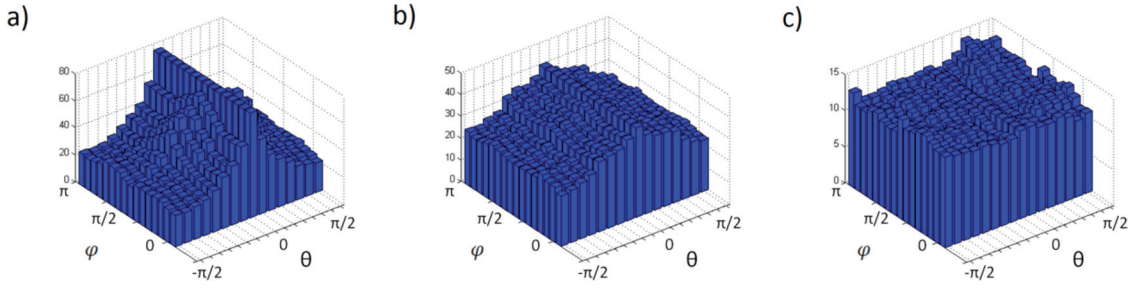


**Figure 13.** Variance of the chord length distribution in dependence of the direction $\alpha = (\theta, \varphi)$ (spherical coordinates). a) Experimental 167 nm film. b) Multiscale sphere model. c) Simulated annealing.

from 500 to 5250 rpm. In agreement with experimental image data,[6] there is a general trend for the morphology to become coarser (i.e., larger separated domains of both polymer and ZnO) for increasing $\omega$, especially for $\omega > 4000$ rpm. Several structural and physical characteristics of the simulated images have been considered. In particular, it was found that the exciton quenching efficiency $\eta_Q$ is monotonically decreasing with increasing $\omega$. More precisely, quenching efficiency decreases from 0.79 for $\omega = 1000$ rpm to 0.18 for for $\omega = 5250$ rpm. This decrease is caused by an increase of spherical contact distances as well as a decrease of volume fraction. Surprisingly, the connectivity of the ZnO phase remained quite high for all spin-coating velocities, indicating that the existence of percolation pathways towards the electrodes is not the limiting factor. Finally, the multiscale sphere model has been compared to simulated annealing.[8] In terms of both structural and physical characteristics, the multiscale sphere model appears to be more suitable to describe the morphology of P3HT-ZnO solar cells.

## Acknowledgements

This research has been supported by Deutsche Forschungsgemeinschaft (DFG) under the Priority Programme: "Elementary Processes of Organic Photovoltaics" (SPP 1355). L.J.A.K. acknowledges support by a grant from STW/NWO (VENI 11166). The work of S.D.O. was further supported by a TOP grant of the Chemical Sciences (CW) division of the Netherlands Organization for Scientific Research (NWO) and is part of the Joint Solar Programme (JSP).

Received: September 4, 2011
Published online: January 26, 2012

[1] Y. Liang, Z. Xu, J. Xia, S.-T. Tsai, Y. Wu, G. Li, C. Ray, L. Yu, *Adv. Mater.* **2010**, *22*, E135.
[2] J. Weickert, R. B. Dunbar, H. C. Hesse, W. Wiedemann, L. Schmidt-Mende, *Adv. Mater.* **2011**, *23*, 1810.
[3] R. Giridharagopal, D. S. Ginger, *J. Phys. Chem. Lett.* **2010**, *1*, 1160.
[4] A. J. Moulé, K. Meerholz, *Adv. Funct. Mater.* **2009**, *19*, 3028.
[5] O. Stenzel, H. Hassfeld, R. Thiedmann, L. J. A. Koster, S. D. Oosterhout, S. S. van. Bavel, J. Loos, M. M. Wienk, R. A. J. Janssen, V. Schmidt, *Ann. Appl. Stat.* **2011**, *5*, 1920.
[6] S. D. Oosterhout, M. M. Wienk, S. S. van Bavel, R. Thiedmann, L. J. A. Koster, J. Gilot, J. Loos, V. Schmidt, R. A. J. Janssen, *Nat. Mater.* **2009**, *8*, 818.
[7] K. Norrman, A. Ghanbari-Siahkali, N. B. Larsen, *Annu. Rep. Prog. Chem., Sect. C* **2005**, *101*, 174.
[8] P. Peumans, S. Uchida, S. R. Forrest, *Nature* **2003**, *425*, 158.
[9] S. S. v. Bavel, E. Sourty, G. de With, J. Loos, *Nano Lett.* **2009**, *9*, 507.
[10] D. Stoyan, W. S. Kendall, J. Mecke, *Stochastic Geometry and its Applications*, 2nd ed., John Wiley & Sons, Chichester **1995**.
[11] J. Illian, A. Penttinen, H. Stoyan, D. Stoyan, *Statistical Analysis and Modeling of Spatial Point Patterns*, John Wiley & Sons, Chichester **2008**.
[12] R. Thiedmann, H. Hassfeld, O. Stenzel, L. J. A. Koster, S. D. Oosterhout, S. S. van Bavel, J. Loos, M. M. Wienk, R. A. J. Janssen, V. Schmidt, *Image Anal. Stereol.* **2011**, *30*, 19.
[13] L. J. A. Koster, *Phys. Rev. B.* **2010**, *81*, 205318.
[14] P. E. Shaw, A. Ruseckas, I. D. W. Samuel, *Adv. Mater.* **2008**, *20*, 3516.
[15] P. Watkins, A. Walker, G. Verschoor, *Nano Lett.* **2005**, *5*, 1814.
[16] R. A. Marsh, C. Groves, N. C. Greenham, *J. Appl. Phys.* **2007**, *101*, 083509.
[17] C. Groves, L. J. A. Koster, N. C. Greenham, *J. Appl. Phys.* **2009**, *105*, 094510.